RSC Advances

PAPER

View Article Online
View Journal | View Issue

Cite this: *RSC Adv.*, 2026, **16**, 19499

Hierarchical ZIF-67@NiS grown on nickel foam as a high-performance binder-free electrode for electrochemical capacitors

Fowzia S. Alamro,[a] Mahmoud A. Hefnawy, *[b] Hoda A. Ahmed[c] and Shymaa S. Medany *[b]

Hierarchical ZIF-67@NiS grown on nickel foam (ZIF-67@NiS-NiF) was successfully synthesized and evaluated as a binder-free electrode for electrochemical capacitor applications. The hybrid architecture integrates the high surface area and redox activity of ZIF-67 with the good electrical conductivity of NiS and the three-dimensional porous framework of Ni foam, facilitating fast charge transfer and efficient ion diffusion. Structural and surface analyses, including XRD, FT-IR, UV-Vis spectroscopy, thermal analysis, SEM, EDXA, and contact angle measurements, confirmed the successful formation, uniform elemental distribution, and enhanced wettability of the composite electrode. Electrochemical studies demonstrated a high specific capacitance of 912 F g^{-1} at 1 A g^{-1}, good rate capability with 74.6% capacitance retention at 10 A g^{-1}, and excellent cycling stability, retaining 89% of its initial capacitance after 10 000 charge–discharge cycles. Kinetic investigations based on electrochemical impedance spectroscopy showed a low charge-transfer resistance and reduced ion-diffusion resistance, while scan-rate-dependent cyclic voltammetry analysis indicated a dominant capacitive-controlled process with fast redox kinetics. The superior capacitive performance is attributed to the synergistic interaction between ZIF-67 and NiS and the interconnected porous structure of the Ni foam substrate, highlighting the strong potential of ZIF-67@NiS-NiF for high-performance energy storage applications.

Received 11th February 2026
Accepted 31st March 2026

DOI: 10.1039/d6ra01220e

rsc.li/rsc-advances

1 Introduction

Energy is the foundation of modern society, driving economic growth, technological advancement, and improved quality of life.[1–3] However, increasing energy demand, depletion of fossil fuels, and environmental impacts pose serious global challenges.[4,5] Transitioning to sustainable and renewable energy sources is essential to ensure energy security and mitigate climate change.[6] Renewable energy is derived from natural resources such as sunlight, wind, water, and biomass that are continuously replenished.[7,8] It offers a clean and sustainable alternative to fossil fuels, reducing greenhouse gas emissions and environmental pollution. Expanding renewable energy technologies is crucial for achieving long-term energy security and sustainable development.[9–11]

Energy storage plays a vital role in balancing energy supply and demand, especially for intermittent renewable sources. Technologies such as batteries, supercapacitors, and hydrogen storage enable efficient utilization of generated energy. Advanced energy storage systems are essential for grid stability and a sustainable energy future.[12–16]

Capacitors are classified into several types, including ceramic, electrolytic, tantalum, film, and supercapacitors, based on their dielectric materials and structure. Each type differs in capacitance range, voltage rating, and application.[17,18] The selection of a capacitor depends on performance requirements such as energy density, stability, and lifetime.[19] Electrochemical capacitors, also known as supercapacitors, store energy through charge separation and fast surface redox reactions at the electrode–electrolyte interface. They offer high power density, rapid charge–discharge capability, and long cycle life compared to conventional capacitors.[20,21]

Zeolitic imidazolate frameworks (ZIFs) are promising materials for electrochemical capacitors due to their high surface area and porous structure, which enhance charge storage.[22,23] ZIFs and their derived carbon or metal oxide materials show improved capacitance, fast ion transport, and good cycling stability.[24]

Hosseinian *et al.* synthesized an rGO/ZIF-67 nanocomposite *via* a simple ultrasonic method, showing enhanced electrochemical performance with a specific capacitance of 210 F g^{-1} and improved conductivity compared to ZIF-67. The composite also exhibited excellent cycling stability (80% after 1000 cycles), making it a promising electrode for supercapacitor applications.[25]

[a]*Department of Chemistry, College of Science, Princess Nourah Bint Abdulrahman University, P.O. Box 84428, Riyadh 11671, Saudi Arabia*
[b]*Chemistry Department, Faculty of Science, Cairo University, 12613-Giza, Egypt. E-mail: shymaasamir80@cu.edu.eg; maadel@cu.edu.eg*
[c]*Department of Chemistry, College of Science in Yanbu, Taibah University, Yanbu Governorate, Saudi Arabia*

Reddy *et al.* developed a phase-controlled CoS_2@gC/rGO nanocomposite *via* a sacrificial ZIF-67 template, achieving a high specific capacitance of 1188 F g^{-1} and excellent coulombic efficiency. An all-solid-state asymmetric supercapacitor using this material delivered high energy and power densities with good long-term cycling stability, highlighting its practical potential.[26]

Nickel sulfide (NiS) coated on nickel foam combines the high conductivity and porous 3D structure of Ni foam with the pseudocapacitive behavior of NiS, leading to enhanced charge storage performance.[27,28] This integrated architecture provides a large active surface area, efficient electron transport, and improved capacitance with good cycling stability for electrochemical capacitor applications.[29,30]

Nandhini *et al.* synthesized NiS nanostructures using microwave, hydrothermal, and combined microwave–hydrothermal methods, with the MH sample exhibiting the highest specific capacitance of 964 F g^{-1} and a low charge transfer resistance. A symmetric supercapacitor using MH exhibited good energy and power densities along with excellent cycling stability, demonstrating its potential as a supercapacitor electrode.[31]

Asghar *et al.* synthesized NiS, ZnS, and NiS/ZnS composites *via* a surfactant-assisted hydrothermal method, with the NiS/ZnS composite exhibiting the highest specific capacitance of 1594.68 F g^{-1}. The composite also demonstrated excellent cycling stability (95.4% after 3000 cycles), indicating its promise as a pseudocapacitor electrode.[32]

In this study, nickel foam was first functionalized with sulfur atoms to form NiS. Subsequently, the NiS surface was modified with ZIF-67 to enhance its electrochemical activity for capacitor applications. The prepared materials were characterized using various analytical techniques, and their electrochemical performance was systematically evaluated using different electrochemical methods to assess their suitability as electrodes for electrochemical capacitors.

2 Experiments section

2.1 Preparation of NiS-NiF

Nickel sulfide (NiS) was synthesized on nickel foam (Ni foam) *via* a reflux method using thiourea as the sulfur source with well-defined quantities. Typically, a piece of Ni foam (2×3 cm^2, thickness ~1.6 mm) was first cleaned by ultrasonication in 1.0 M HCl for 15 min, followed by ethanol and deionized water for 10 min each. For the sulfurization process, 0.76 g of thiourea (10 mmol) was dissolved in 50 mL of deionized water under stirring to form a clear solution. The cleaned Ni foam was then immersed in the solution, and the mixture was heated under reflux at ~120 °C for 4 h. During reflux, thiourea decomposed gradually, releasing S^{2-} ions that reacted with surface Ni to form NiS directly on the foam. After cooling to room temperature, the NiS/NiF electrode was removed, washed thoroughly with deionized water and ethanol, and dried at 60 °C for 6 h.

2.2 Preparation of ZIF-67

ZIF-67 was prepared using a hydrothermal method by reacting cobalt nitrate with 2-methylimidazole in a sealed autoclave. Typically, 1.46 g of $Co(NO_3)_2 \cdot 6H_2O$ (5 mmol) was dissolved in 40 mL of deionized water or methanol to form solution A, while 3.28 g of 2-methylimidazole (40 mmol) was dissolved in 40 mL of the same solvent to form solution B. Solution B was added slowly to solution A under stirring for 20 min to obtain a homogeneous mixture, which was then transferred into a Teflon-lined stainless-steel autoclave and heated at 120 °C for 6 h. After naturally cooling to room temperature, the obtained purple ZIF-67 crystals were collected by centrifugation, washed several times with methanol and deionized water to remove residual reactants, and dried at 60 °C for 12 h. The hydrothermal route promotes improved crystallinity and controlled crystal growth of ZIF-67, making it suitable for advanced catalytic and electrochemical applications.

2.3 Preparation ZIF-67@NiS-NiF

ZIF-67 was grown onto the NiS-modified nickel foam (NiS-NiF) *via* a suspension-based functionalization approach to form a ZIF-67@NiS-NiF composite electrode. In a typical procedure, the as-prepared NiS-NiF was first ultrasonically cleaned in ethanol and deionized water to ensure a clean and activated surface. Separately, ZIF-67 particles were synthesized and then dispersed in methanol to form a stable suspension under ultrasonication. The NiS-NiF substrate was immersed in the ZIF-67 suspension and gently stirred for several hours, allowing the ZIF-67 crystals to uniformly anchor onto the NiS surface through interfacial interactions. After functionalization, the ZIF-67@NiS-NiF electrode was removed from the suspension, thoroughly rinsed with methanol to eliminate weakly attached particles, and dried at 60 °C. This suspension-assisted functionalization strategy enables uniform loading of ZIF-67 on the conductive NiS-Ni foam framework, providing abundant exposed active sites and enhanced charge-transfer pathways suitable for electrochemical applications.

2.4 Electrochemical measurement

Electrochemical measurements were carried out using an AUTOLAB PGSTAT128N potentiostat/galvanostat in a conventional three-electrode configuration. The as-prepared ZIF-67@NiS-NiF electrode was directly used as the working electrode without any binder or conductive additive. A platinum wire served as the auxiliary (counter) electrode, while an Ag/AgCl electrode (3.0 M KCl) was employed as the reference electrode. All electrochemical tests were conducted at room temperature, and the potential reported in this work are referenced to the Ag/AgCl electrode unless otherwise specified. This configuration ensures reliable evaluation of the intrinsic electrochemical behavior of the ZIF-67@NiS-NiF electrode.

3 Results and discussion

3.1 Structural and surface characterization

The X-ray diffraction (XRD) patterns of pristine nickel foam (NiF), NiS-modified Ni foam (NiS-NiF), ZIF-67 grown on NiS-NiF (ZIF-67@NiS-NiF), and pure ZIF-67 are presented in Fig. 1a. For the pristine Ni foam, characteristic peaks appear at $2\theta = 44.26°$,

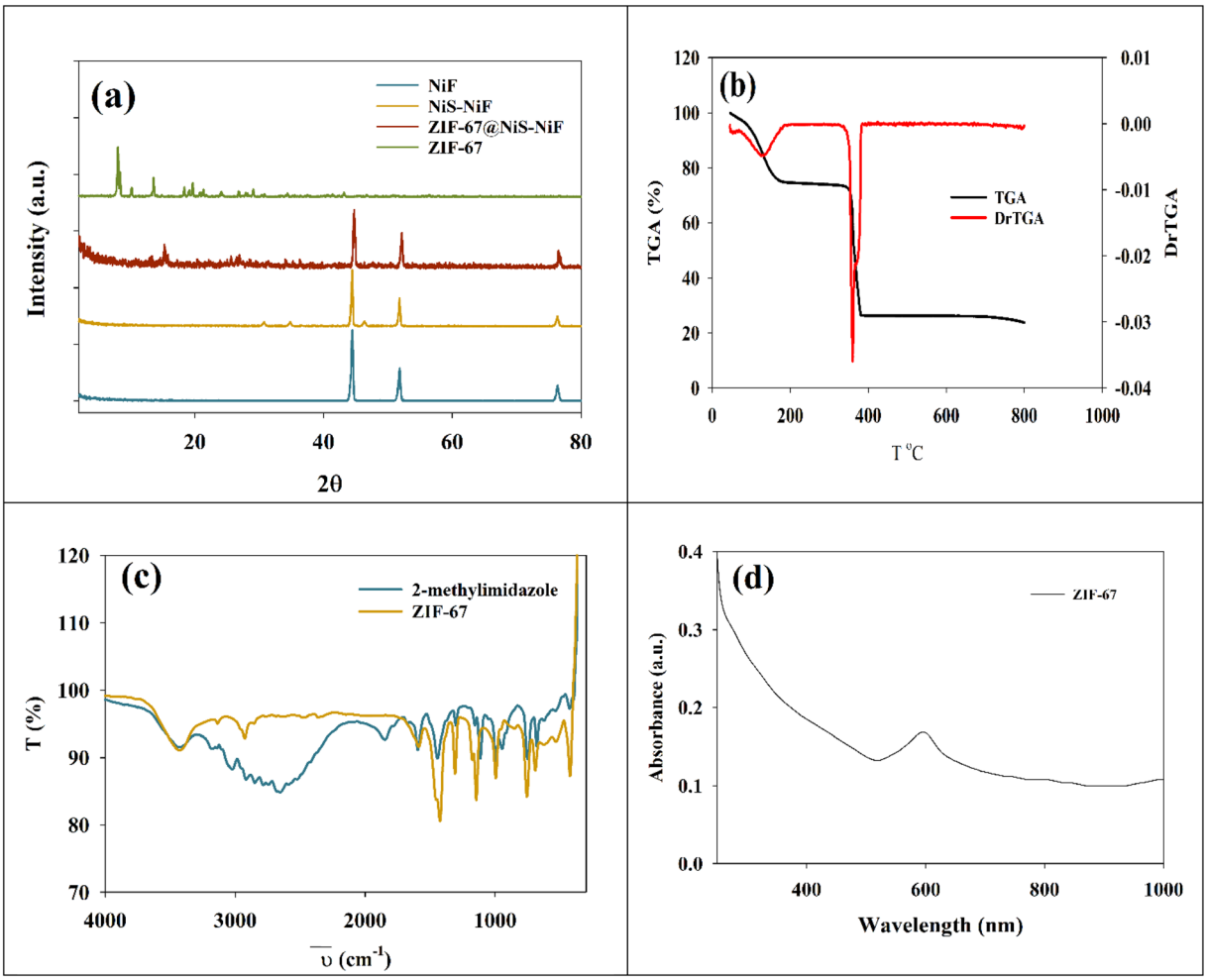

Fig. 1 (a) XRD of different prepared materials, (b) thermal analysis of ZIF-67, (c) FT-IR of ZIF-67 and 2 methylimidazole, (d) UV-Vis of ZIF-67.

51.56°, and 76.22°, corresponding to the (111), (200), and (220) planes of face-centered cubic (fcc) nickel (JCPDS No. 04-0850). These sharp and intense peaks indicate a highly crystalline Ni framework, which serves as an excellent conductive substrate for further modifications.[33] Upon deposition of NiS onto the Ni foam (NiS-NiF), additional diffraction peaks emerge at 2θ = 30.9°, 35.1°, and 46.6°, which can be indexed to the (100), (101), and (102) planes of hexagonal NiS (JCPDS No. 02-1280). The Ni peaks remain visible, confirming that the underlying Ni foam maintains its crystalline structure after sulfide growth.[34] The growth of ZIF-67 on NiS-NiF (ZIF-67@NiS-NiF) introduces new peaks characteristic of the Co-based zeolitic imidazolate framework, observed at 2θ = 7.8°, 10.12°, 13.14°,and 18.4°, corresponding to the (011), (002), (112), and (222) planes of ZIF-67.[35,36] These reflections indicate successful integration of the ZIF-67 crystals on the NiS-coated foam, while the Ni and NiS peaks remain detectable, confirming that the substrate and sulfide layer are still intact.

Thermogravimetric (TGA) and derivative thermogravimetric (DrTGA) analyses were performed to evaluate the thermal stability and decomposition behavior of the ZIF-67 sample, as represented in Fig. 1b. The TGA/DrTGA curves reveal three distinct weight-loss stages. The first DrTGA peak appears at approximately 49.6 °C, with a slight mass loss of about 3%, which is attributed to the removal of physically adsorbed water and residual solvent molecules weakly held within the porous framework.[37] The second weight-loss step occurs in the temperature range of 90–164 °C, showing a more pronounced mass decrease of nearly 21%, which can be assigned to the release of strongly confined guest molecules and the initial decomposition of the organic 2-methylimidazolate ligands. The third and major DrTGA peak is observed between 344 and 385 °C, accompanied by a substantial weight loss of approximately 48%, corresponding to the complete decomposition of the organic framework and the collapse of the ZIF-67 structure. Beyond this temperature range, the remaining mass is associated with thermally stable cobalt-containing residues, confirming the thermal decomposition pathway of ZIF-67.[38,39]

Fig. 1c shows the FT-IR spectrum of 2-methylimidazole with characteristic bands confirming its molecular structure. The broad band at 3100–3400 cm^{-1} is assigned to N–H stretching, while the weak bands at 2920–2850 cm^{-1} correspond to C–H stretching of the methyl group. A strong band observed at 1580–1620 cm^{-1} is attributed to the C=N stretching vibration of the imidazole ring. The absorption bands in the 1100–1250 cm^{-1} region are related to C–N stretching, and the peaks appearing at

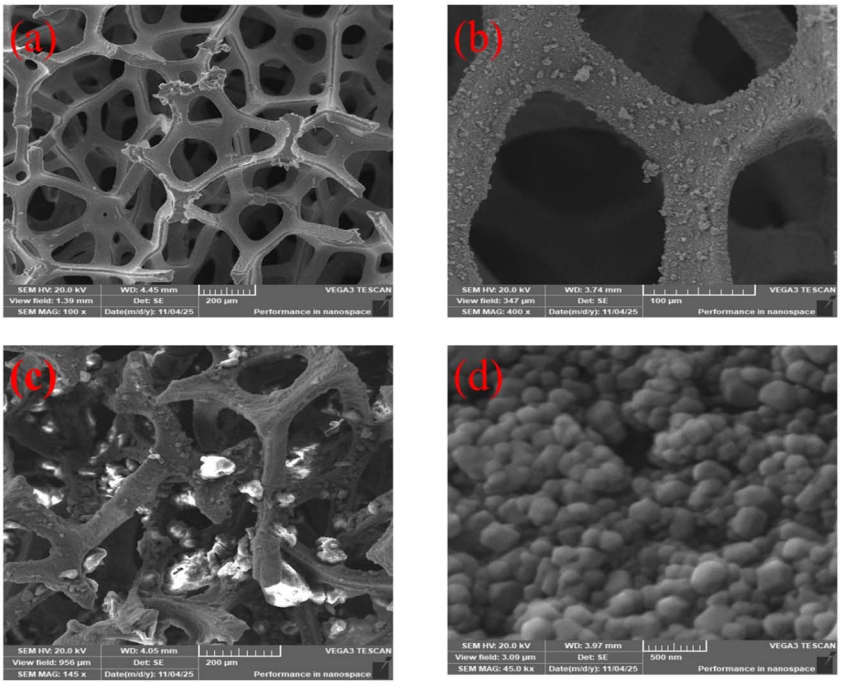

Fig. 2 SEM of surfaces (a) pristine Ni foam, (b) NiS-NiF, (c)ZIF-67@NiS-NiF, (d) pristine ZIF-67.

700–900 cm^{-1} are associated with out-of-plane bending vibrations, confirming the aromatic heterocyclic nature of 2-methylimidazole. Overall, the spectrum in Fig. 1c agrees well with reported data, verifying the successful identification of 2-methylimidazole as an organic linker.[40–42]

The FT-IR spectrum of ZIF-67, which presented in Fig. 1c, confirms the successful formation of the metal–organic framework. The characteristic bands of the imidazolate linker are retained, with the C=N stretching vibration appearing around 1580–1600 cm^{-1}, indicating the preservation of the imidazole ring after coordination. The absorption bands in the 1100–1250 cm^{-1} region are attributed to C–N stretching vibrations, further supporting the presence of the organic linker within the framework.[43,44]

Compared with free 2-methylimidazole, the slight shift and reduced intensity of the N–H band in the 3100–3400 cm^{-1} region indicate deprotonation and coordination of nitrogen atoms with Co^{2+} ions. A new absorption band observed in the 420–450 cm^{-1} region is assigned to the Co–N stretching vibration, providing direct evidence for metal–ligand bond formation. Additionally, the bands at 2920–2850 cm^{-1} correspond to C–H stretching of the methyl groups, confirming the structural integrity of the linker.

The UV-Vis absorption spectrum of ZIF-67 shows a single prominent absorption band centered around ~600 nm, which is attributed to the d–d electronic transitions of Co^{2+} ions in a tetrahedral coordination environment within the ZIF-67 framework (see Fig. 1d). This characteristic peak confirms the successful coordination of cobalt ions with the 2-methylimidazolate ligands and the formation of the ZIF-67 structure.[45]

Fig. 2 illustrates the morphological evolution of the electrode surface at different preparation stages, highlighting changes in

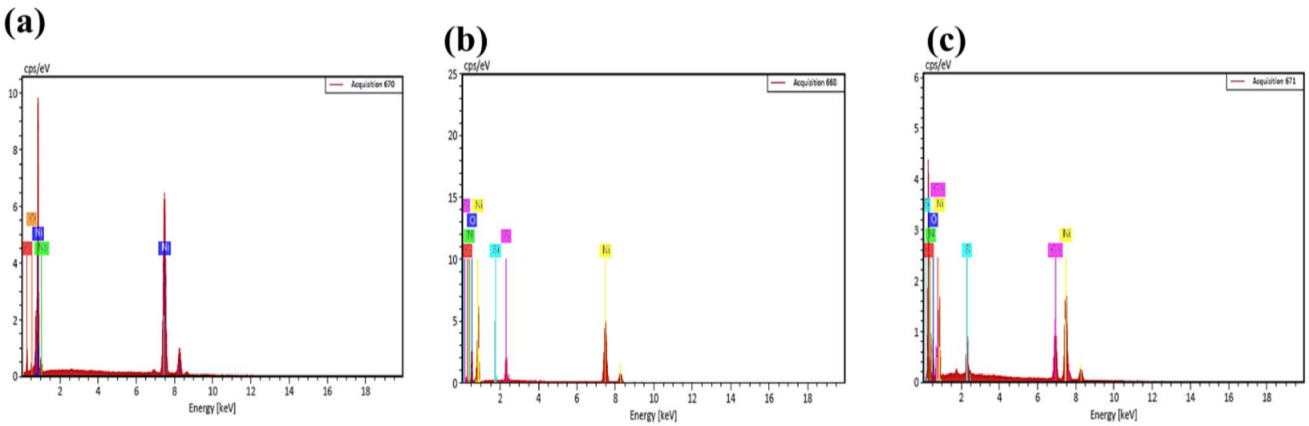

Fig. 3 EDAX of prepared materials (a) NiF, (b) NiS-NiF, (c) ZIF-67@NiS-NiF.

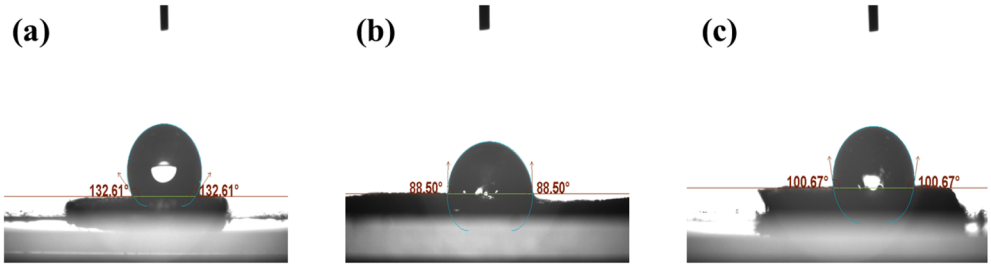

Fig. 4 Contact angle of surfaces (a) NiF, (b) NiS-NiF, (c) ZIF-67@NiS-NiF.

surface area, texture, and particle distribution. Fig. 2a shows the SEM image of pristine Ni foam, which exhibits a typical three-dimensional porous network composed of interconnected nickel ligaments with smooth surfaces. This open macroporous structure provides a large geometric surface area and efficient pathways for electrolyte penetration and electron transport, making Ni foam an ideal current collector for electrochemical applications.

After sulfurization, the SEM image of NiS-NiF (see Fig. 2b) reveals a significant change in surface morphology. The originally smooth Ni ligaments become roughened and uniformly covered with a dense NiS layer, forming nanoscale features distributed over the foam skeleton. This rough and textured surface markedly increases the effective surface area and generates abundant exposed active sites, while the conformal growth of NiS ensures intimate contact with the conductive Ni foam substrate.

Fig. 2c represents the SEM image of ZIF-67@NiS-NiF, where ZIF-67 particles are clearly observed to be homogeneously distributed on the NiS-coated Ni foam surface. The ZIF-67 crystals are well anchored onto the NiS layer without severe agglomeration, indicating successful functionalization *via* suspension deposition. The hierarchical architecture, combining the porous Ni foam backbone, the rough NiS interlayer, and the uniformly dispersed ZIF-67 particles, greatly enhances the accessible surface area and facilitates efficient electrolyte diffusion. This uniform particle distribution also promotes effective charge transfer across the interfaces.

For comparison, Fig. 2d shows the SEM image of pristine ZIF-67, which displays well-defined polyhedral crystals with relatively uniform size and smooth facets. While ZIF-67 alone possesses intrinsic microporosity and high surface area, its integration onto the NiS-NiF framework prevents particle aggregation and maximizes the utilization of its active surface.

Fig. 3 presents the EDAX results confirming the elemental composition and successful stepwise modification of the electrode surface. Fig. 3a shows the EDAX spectrum of pristine Ni foam, which is dominated by a strong Ni signal, indicating the high purity of the nickel substrate, with only minor signals of oxygen attributed to surface oxidation and atmospheric exposure. This result confirms that the Ni foam serves as a clean and conductive current collector.

As shown in Fig. 3b, the EDAX spectrum of NiS-NiF reveals the clear presence of sulfur in addition to nickel, confirming the successful sulfurization of the Ni foam surface and the formation of NiS. The relatively uniform Ni and S signals suggest a homogeneous distribution of NiS across the foam framework, while the slight oxygen signal can be ascribed to surface oxidation or adsorbed species.

Fig. 3c displays the EDAX spectrum of ZIF-67@NiS-NiF, where, in addition to Ni and S, distinct Co, C, and N signals are observed. The appearance of cobalt confirms the successful incorporation of ZIF-67 onto the NiS-modified Ni foam, while the carbon and nitrogen signals originate from the 2-methylimidazole organic linker of ZIF-67. The simultaneous detection of Ni, S, Co, C, and N verifies the formation of a composite architecture and indicates that ZIF-67 is well anchored on the NiS-NiF surface, supporting the SEM observations of uniform particle distribution and effective surface functionalization.

Fig. 4 illustrates the contact angle measurements used to evaluate the surface wettability of the electrodes at different modification stages and its impact on electrochemical performance. As shown in Fig. 4a, pristine Ni foam exhibits a high contact angle of 132.6°, indicating a highly hydrophobic surface. Such poor wettability limits electrolyte penetration into the porous structure, thereby reducing the effective electrochemically active surface area.

After sulfurization, the NiS-NiF (Fig. 4b) shows a markedly reduced contact angle of 88.5°, reflecting a significant improvement in surface hydrophilicity. This behavior can be attributed to the formation of polar Ni–S bonds and the increased surface roughness induced by the NiS layer, which together enhance the affinity of the surface toward the aqueous electrolyte. Improved wettability facilitates faster electrolyte diffusion and more efficient ion transport to the active sites, which is highly beneficial for charge storage processes in electrochemical capacitors.

Following ZIF-67 functionalization, the contact angle slightly increases to 100.67° (Fig. 4c), indicating a moderate reduction in hydrophilicity compared to NiS-NiF. This change is associated with the presence of organic 2-methylimidazole linkers in ZIF-67, which introduce relatively hydrophobic components to the surface. Nevertheless, the contact angle remains substantially lower than that of pristine Ni foam, suggesting that the composite electrode still maintains acceptable wettability. Importantly, the hierarchical porous structure of ZIF-67@NiS-Ni foam provides abundant ion-accessible channels and a large interfacial area, compensating for the slight decrease in hydrophilicity.

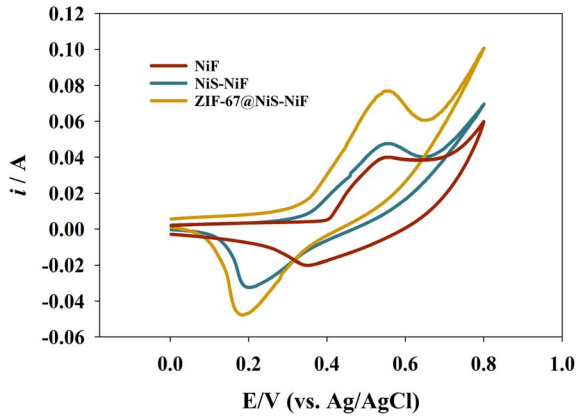

Fig. 5 Comparison between different Ni foam modified surfaces behavior in 1.0 M NaOH solution.

3.2 Electrochemical capacitance of ZIF-67@NiS-NiF

Fig. 5 presents the cyclic voltammograms (CVs) of bare nickel foam (NiF), NiS-modified nickel foam (NiS-NiF), and ZIF-67@NiS-NiF electrodes recorded in 1.0 M NaOH at a scan rate of 20 mV s^{-1}. All CV curves exhibit a pair of well-defined redox peaks, which are characteristic of the reversible faradaic reactions associated with the Ni(II)/Ni(III) redox couple, confirming the pseudocapacitive behavior of the investigated electrodes.

The anodic peak corresponds to the oxidation of Ni(II) to Ni(III), while the cathodic peak is attributed to the reverse reduction process. These redox reactions can be described by the following equation:

$$Ni(OH)_2 + OH^- \rightleftharpoons NiOOH + H_2O + e^- \quad (1)$$

Among the three electrodes, bare NiF shows the lowest current response and smallest enclosed CV area, indicating limited electroactive surface area and sluggish redox kinetics. Upon sulfurization, the NiS-NiF electrode exhibits a significant increase in both anodic and cathodic peak currents, which can be attributed to the improved electrical conductivity and enhanced electrochemical activity introduced by the NiS layer.

Additionally, the ZIF-67@NiS-NiF electrode demonstrates the highest redox peak currents and the largest CV enclosed area, reflecting its superior charge storage capability. This enhancement arises from the synergistic effect between ZIF-67 and NiS, where the porous ZIF-67 framework provides abundant electroactive sites and facilitates electrolyte penetration, while NiS ensures efficient electron transport. Additionally, the hierarchical architecture grown on the three-dimensional Ni foam promotes rapid ion diffusion and accelerates the Ni(II)/Ni(III) redox transitions.

Fig. 6a presents the cyclic voltammograms (CVs) of the ZIF-67@NiS-NiF electrode recorded in 1.0 M NaOH at different scan rates ranging from 2 to 60 mV s^{-1}. As the scan rate increases, a pronounced increase in both anodic and cathodic current responses is observed, indicating enhanced electrochemical activity and efficient utilization of electroactive sites at higher sweep rates. The well-defined redox peaks appearing in all CV curves confirm the dominance of faradaic redox reactions associated with the Ni^{2+}/Ni^{3+} redox couple, which plays a key role in the charge-storage process. With an increasing scan rate, the anodic peak potential gradually shifts toward more positive values, while the cathodic peak potential shifts toward more negative values, reflecting increased polarization and internal resistance effects at higher sweep rates. This peak separation suggests that the redox process is quasi-reversible rather than ideally reversible, as the system requires additional overpotential to drive the electron-transfer reaction at faster scan rates. Nevertheless, the retention of the redox peak shapes and their proportional current increase across the entire scan rate range indicate good electrochemical reversibility and fast reaction kinetics.

The charge-storage mechanism of the ZIF-67@NiS-NiF electrode was further elucidated using the Trasatti method, which enables the quantitative separation of surface-controlled and diffusion-controlled charge contributions. According to the Trasatti relation:

$$q = q_\infty + a\nu^{-0.5} \quad (2)$$

The linear dependence of the voltametric charge (q) on $\nu^{-0.5}$confirms the coexistence of two distinct charge-storage processes (see Fig. 6b). Here, q_∞represents the charge associated with the outer, electrochemically accessible surface, while

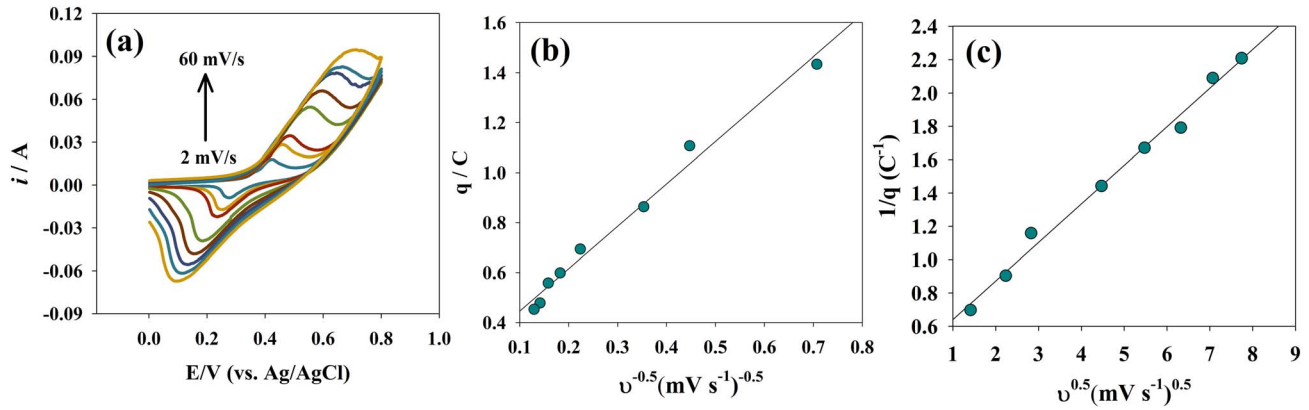

Fig. 6 (a) CVs of ZIF-67@NiS-NiF at different scan rates, (b) relation between $\nu^{-0.5}$ *vs.* q, (c) relation between $\nu^{0.5}$ *vs.* $1/q$.

the second term corresponds to diffusion-controlled charge originating from inner active sites. From the linear fitting, a q_∞value of 0.276 C was obtained, indicating a substantial contribution from fast surface redox reactions. This behavior highlights the efficient utilization of both outer and inner electroactive sites, confirming a mixed charge-storage mechanism.

As illustrated in Fig. 6c, further validating this analysis, the Trasatti method was also applied using the inverse relationship:

$$1/q = 1/q_t + bv^{0.5} \quad (3)$$

where q_t denotes the total charge stored at infinitely slow scan rates. The linear variation of $1/q$ with $v^{0.5}$ confirms the reliability of the Trasatti approach for the present system. From the intercept of the linear fit, a total charge value of $q_t = 2.48$ C was obtained. Using these values, the contribution of diffusion-controlled charge can be estimated as $q_{diff} = q_t - q_\infty$, yielding approximately 2.2 C, which corresponds to about 88.87% of the total stored charge. Therefore, the percentage of the outer (surface faradaic and EDLCs) to the inner (bulk faradaic) is 11.13%. These findings are in excellent agreement with the b-value analysis, scan-rate dependence, and diffusion coefficient results, further confirming the highly efficient, mixed-charge-storage behavior of the electrode for electrochemical capacitor applications.

The variation of anodic and cathodic peak current densities with scan rate for the ZIF-67@NiS-NiF electrode exhibits a clear linear relationship, as illustrated in Fig. 7a, confirming that the redox process is predominantly surface-controlled rather than diffusion-limited. This behavior indicates that the electroactive species are strongly confined to the electrode surface and actively contribute to charge storage. For a surface-confined process, the peak current density (j_p) is related to the scan rate (v) by the following equation:[46]

$$j_p = n^2F^2\Gamma v/4RT \quad (4)$$

Based on the linear fitting of the anodic and cathodic current density *versus* scan rate plots shown in Fig. 6a, the surface coverage (Γ) values were calculated separately from the corresponding slopes, and an average surface coverage was then determined to provide a more reliable representation of the electrochemically active sites. The averaged surface coverage was found to be 1.65×10^{-7} mol cm^{-2}, indicating a high density of accessible redox-active sites on the ZIF-67@NiS-NiF surface. This high Γ value can be attributed to the synergistic integration of the porous ZIF-67 framework with the conductive NiS layer supported on three-dimensional nickel foam, which enhances surface accessibility, electrical conductivity, and charge-transfer kinetics. Consequently, the high average surface coverage explains the pronounced capacitive behavior and confirms the suitability of the ZIF-67@NiS-NiF electrode for high-performance electrochemical capacitor applications.

The relationship between the anodic and cathodic peak current densities and the square root of scan rate ($v^{1/2}$) for the ZIF-67@NiS-NiF electrode shows a clear linear dependence, as presented in Fig. 7b, indicating that the redox process is governed by a diffusion-controlled mechanism. This behavior suggests that, in addition to surface-confined contributions, ion diffusion within the porous electrode structure plays an important role in the electrochemical response. The diffusion coefficient (D) was estimated using the Randles–Ševčík equation for a reversible system expressed in terms of current density:[47,48]

$$j_p = 2.69 \times 10^5 n^{3/2}D^{1/2}Cv^{1/2} \quad (5)$$

where n is the number of electrons transferred ($n = 1$), $C$is the electrolyte concentration, and is the scan rate. From the linear fitting of the anodic and cathodic plots in Fig. 7b, a slope was obtained. Assuming an electrolyte concentration of 1.0 M, the diffusion coefficient was calculated to be approximately 2.05×10^{-5} cm^2 s^{-1}. This relatively high diffusion coefficient reflects efficient ion transport within the hierarchical ZIF-67@NiS-NiF architecture, which benefits from the porous ZIF-67 framework, the conductive NiS layer, and the three-dimensional nickel foam substrate. The enhanced diffusion kinetics, together with the high surface coverage discussed previously, explain the electrode's superior electrochemical performance and further confirm its suitability for high-performance electrochemical capacitor applications.

The electrochemical evidence for a mixed charge-storage mechanism in the ZIF-67@NiS-NiF electrode was further evaluated by analyzing the relationship between the logarithm of peak current density and the logarithm of the scan rate, as shown in Fig. 7c. This analysis is based on the power-law equation:

$$I = av^b \quad (6)$$

where parameter b provides insight into the dominant charge-storage process. A b value close to 0.5 is characteristic of a diffusion-controlled process, whereas a value approaching 1.0 indicates a surface-controlled (capacitive) mechanism. From the linear fitting of the log(j) *versus* log(v) plot in Fig. 6c, a b value of 0.508 was obtained, which is very close to the theoretical value of 0.5. This result clearly suggests that the electrochemical behavior of the ZIF-67@NiS-NiF electrode is predominantly diffusion-controlled, while still maintaining a contribution from surface-confined redox reactions. The coexistence of these two mechanisms confirms a mixed charge-storage behavior, arising from fast surface redox reactions at the ZIF-67/NiS interface and ion diffusion within the porous electrode matrix. This finding is consistent with the results from the scan-rate dependence and Randles–Ševčík analysis (Fig. 7a and b) and highlights the synergistic role of the porous ZIF-67 structure, the conductive NiS layer, and the three-dimensional nickel foam in enabling efficient ion transport and charge storage.

The dependence of the anodic and cathodic peak potentials on the logarithm of scan rate for the ZIF-67@NiS-NiF electrode is illustrated in Fig. 7d and provides valuable insight into the charge-transfer kinetics and reversibility of the electrochemical

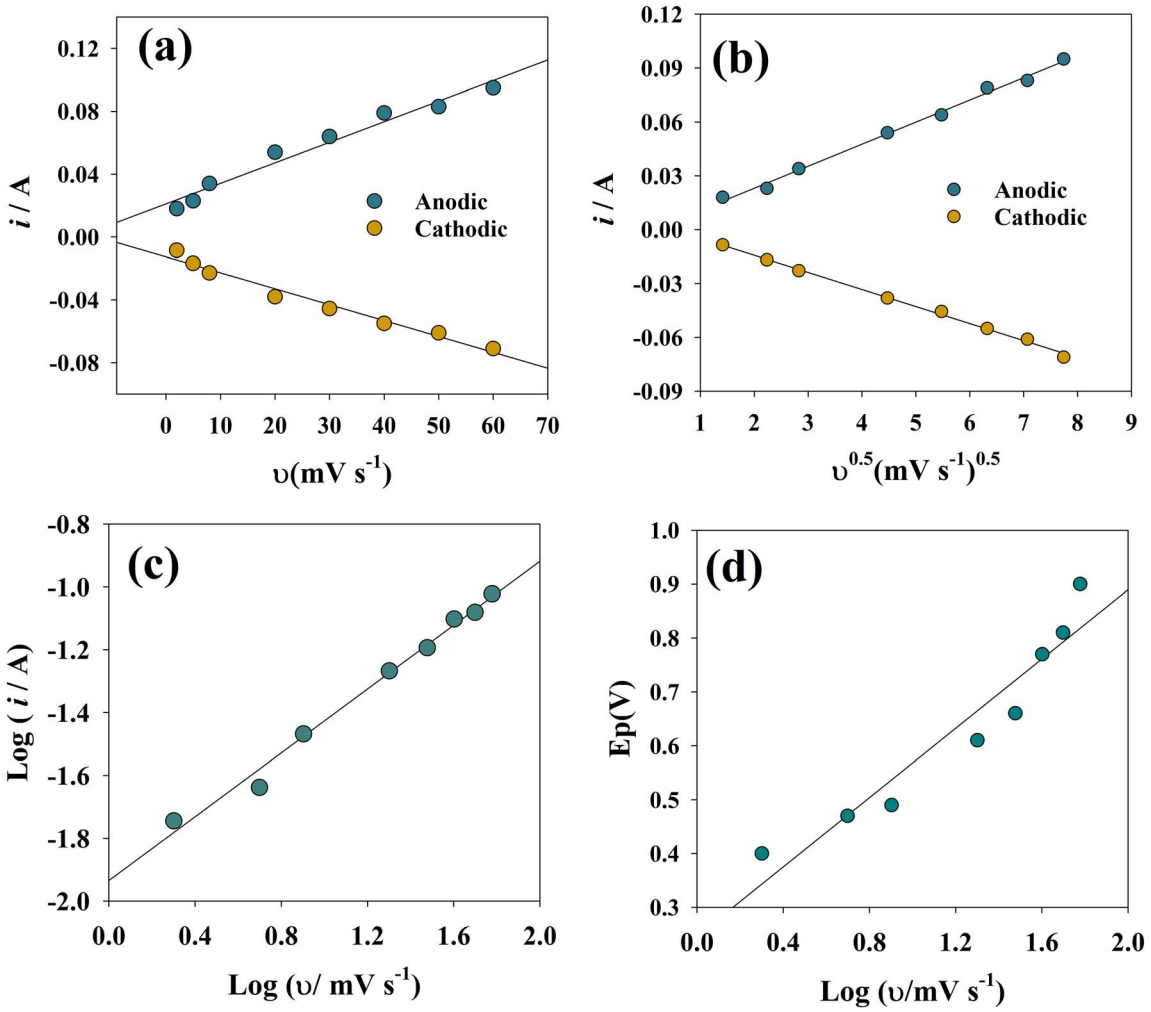

Fig. 7 (a) Relation between scan rate *vs.* current for anodic and cathodic processes, (b) relation between the square root of scan rate *vs.* current for anodic and cathodic processes, (c) relation between the logarithm of scan rate *vs.* the logarithm of current, (d) relation between logarithm of scan rate *versus* peak potential.

process. The linear variation of peak potential with log(ν) indicates a quasi-reversible redox behavior, in which both electron-transfer kinetics and mass transport contribute to the overall electrochemical response. With increasing scan rate, the anodic peak potential shifts toward more positive values, while the cathodic peak shifts toward more negative potentials, reflecting increased polarization and ohmic resistance within the electrode. Such behavior is characteristic of kinetically limited faradaic reactions occurring in porous and nanostructured electrodes. According to Laviron's theory, the linear E_p–log(ν) relationship observed in Fig. 6d confirms that the electrochemical reaction is governed by charge-transfer kinetics at the ZIF-67@NiS-NiF surface. This observation is fully consistent with the mixed charge-storage mechanism revealed by the scan-rate dependence of current (Fig. 7a–c), where both surface-confined redox reactions and diffusion-controlled ion transport coexist.

Fig. 8a shows the GCD curves of the ZIF-67@NiS-NiF electrode measured in 1.0 M NaOH within a 0.5 V potential window at current densities from 1 to 5 A g^{-1}. The curves display nearly symmetric charge–discharge profiles, indicating good reversibility and high coulombic efficiency.

The non-linear GCD shapes confirm a dominant pseudocapacitive behavior arising from Ni-based redox reactions. At 1 A g^{-1}, a longer discharge time is observed due to efficient utilization of electroactive sites. Increasing the current density to 5 A g^{-1} shortens the discharge time because of limited ion diffusion and increased polarization. Notably, the curves maintain similar shapes with a small IR drop, reflecting low internal resistance and good rate capability. These results demonstrate the favorable charge-storage kinetics and electrochemical stability of the ZIF-67@NiS-NiF electrode.

Fig. 8b shows that the specific capacitance of the ZIF-67@NiS-NiF electrode decreases from 912 to 680 F g^{-1} as the current density increases from 1 to 5 A g^{-1}. This trend is typical of pseudocapacitive materials and is primarily due to limited ion diffusion and a shortened discharge time at higher current densities, which restricts the utilization of inner electroactive sites. A comparison between ZIF-67@NiS-NiF and other surfaces reported in the literature is presented in Table 1.

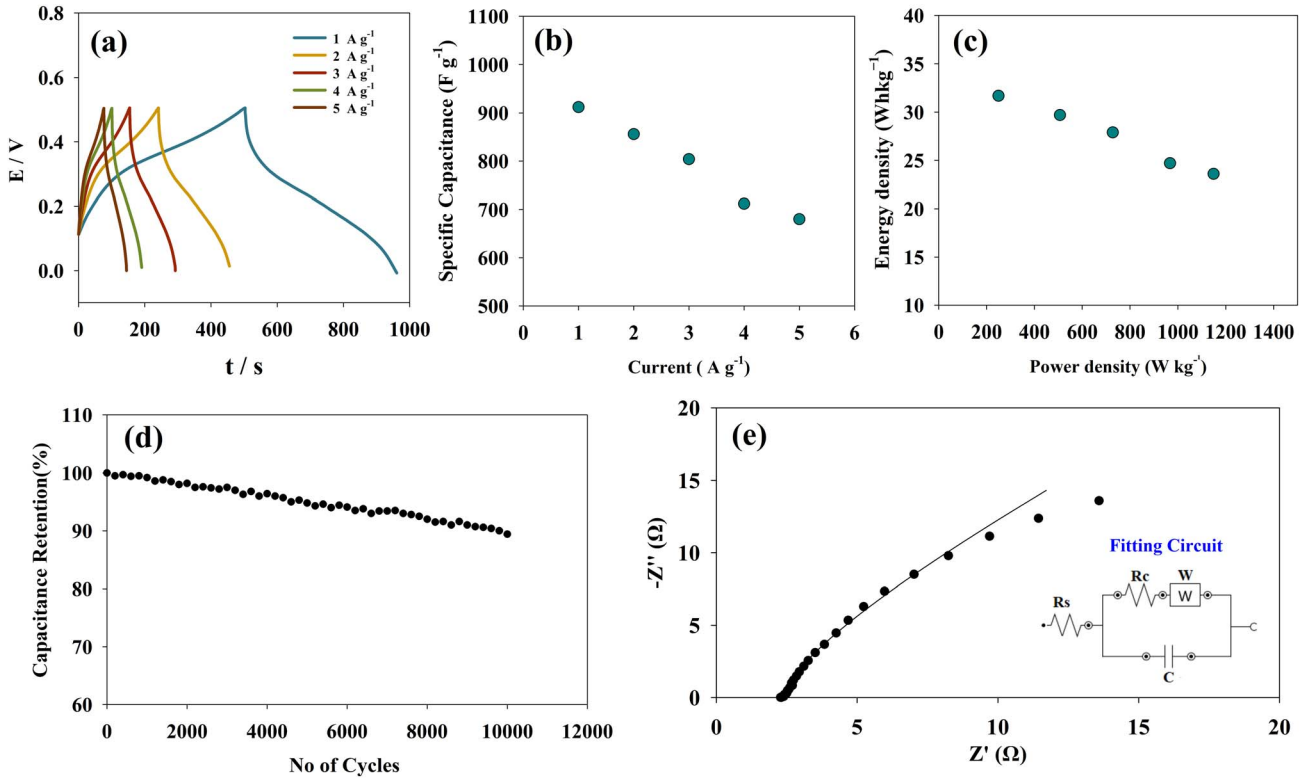

Fig. 8 (a) GCD of the modified ZIF-67@NiS-NiF, (b) relation between current and specific capacitance, (c) region plot, (d) capacitance retention of modified electrode for 10 000 cycles, (e) EIS of the modified electrode at 0.4 V.

At low current density, sufficient time is available for electrolyte ions to access the porous ZIF-67 structure and the redox-active NiS-NiF centers, resulting in high capacitance. At higher current densities, charge storage is dominated by surface reactions, leading to a gradual decline in capacitance. Notably, the electrode retains 74.6% of its initial capacitance at 5 A g^{-1}, indicating good rate capability. This performance reflects the synergistic effect of the porous ZIF-67 framework and the conductive NiS-NiF network, confirming the suitability of ZIF-67@NiS-NiF for high-rate electrochemical capacitor applications.

The Ragone plot of the ZIF-67@NiS-NiF electrode, shown in Fig. 8c, illustrates the relationship between energy density and power density at different current densities. At a low current density of 1 A g^{-1}, the electrode delivers a high energy density of 31.7 Wh kg^{-1} at a power density of 250 W kg^{-1}, reflecting efficient charge storage and full utilization of electroactive sites. With increasing power density, a gradual decrease in energy density is observed, attributed to restricted ion diffusion and reduced discharge time at high rates.

Importantly, as depicted in Fig. 8c, the ZIF-67@NiS-NiF electrode maintains a considerable energy density of 23.6 Wh kg^{-1} even at a high-power density of 1149 W kg^{-1}, demonstrating excellent rate capability and rapid charge–discharge behavior. This outstanding performance is primarily attributed to the synergistic effect between the porous ZIF-67-derived structure and the conductive NiS-modified nickel foam, which enhances electron transport, facilitates electrolyte penetration, and provides numerous accessible redox-active sites.

The long-term cycling stability of the ZIF-67@NiS-NiF electrode was evaluated by repeated charge–discharge measurements at a current density of 1 mA g^{-1} for 10 000 cycles, as shown in Fig. 8d. The electrode exhibits a capacitance retention of 89%, indicating good electrochemical durability under continuous cycling conditions. The gradual decrease in capacitance can be attributed to partial structural deformation,

Table 1 Comparison of surface performance for capacitor applications

Surface	Potential window (V)	Capacitance (F g^{-1})	Rate capability	Durability	References
ZIF-67@NiS-NiF	0.5	912@1 A g^{-1}	74.6% (1 to 5 A g^{-1})	89% (10000 cycles at 5 A g^{-1})	This work
CNFs/MnO_2	1.0	151.1@1 A g^{-1}	76.2% (1–8 A g^{-1})	90% (8000@ 2 A g^{-1})	49
Ni–Co double hydroxide	0.45	1246 F g^{-1} (1 A g^{-1})	91.8% (1 to 10 A g^{-1})	80.1% (1000 cycles at 10 A g^{-1})	50
CoNiFe-layered double hydroxide	0.4	1203 F g^{-1} (1 A g^{-1})	77.1% (1 to 10 A g^{-1})	94% (1000 cycles at 20 A g^{-1})	51
GC/$NiFe_2O_4$@CNT	0.4	1169 (at 5 A g^{-1})	62.4% (5 to 17 A g^{-1})	90.1% (2000 cycles at 10 A g^{-1})	52
CF/$NiMn_2O_4$	0.65	301@ 1 A g^{-1}	69% (1–6 mA cm^{-2})	85% (2000 @5 mA cm^{-2})	53

dissolution of active species, or volume changes associated with repeated Faradaic redox reactions in the alkaline electrolyte. Nevertheless, the relatively high retention after prolonged cycling demonstrates strong interfacial adhesion between ZIF-67, NiS, and the Ni foam substrate, effectively mitigating detachment of the active material. Moreover, the porous architecture of ZIF-67, combined with the conductive NiS framework, facilitates maintaining efficient diffusion and electron transport throughout cycling. These results confirm that the ZIF-67@NiS-NiF electrode possesses acceptable long-term stability, supporting its potential application in practical electrochemical capacitor devices.

Fig. 8e shows the electrochemical impedance spectroscopy (EIS) response of the ZIF-67@NiS-NiF modified electrode measured at an applied potential of 0.4 V. The experimental data were well fitted by an equivalent circuit consisting of the solution resistance (R_s) in series with a parallel combination of the charge transfer resistance (R_c) and capacitance (C), followed by a Warburg diffusion element (W) in series with R_c. This circuit appropriately describes the interfacial charge-transfer and ion-diffusion processes occurring at the electrode–electrolyte interface.

The fitted R_s value of 2 Ω indicates low electrolyte and intrinsic electrode resistance, reflecting good ionic conductivity of the 1.0 M NaOH electrolyte and effective electrical contact between the active material and the Ni foam substrate. The relatively small charge-transfer resistance ($R_c = 14$ Ω) suggests fast electron-transfer kinetics at the ZIF-67@NiS-NiF/electrolyte interface, which can be attributed to the conductive NiS phase and to the intimate integration of the active layer with the three-dimensional Ni foam.

The capacitance value ($C = 4.78 \times 10^{-4}$ F) confirms the electrode's capacitive nature, associated with surface redox reactions and interfacial charge accumulation. Moreover, the presence of a Warburg element with a low coefficient ($W = 1.45 \times 10^{-4}$) indicates minimal diffusion resistance and efficient ion transport within the porous ZIF-67 framework. The series connection of R_c and W highlights that ion diffusion accompanies the charge-transfer process, particularly at lower frequencies.

The low R_s and R_c values, together with the small Warburg impedance, demonstrate favorable charge-transfer kinetics and rapid ion diffusion for the ZIF-67@NiS-NiF electrode. These EIS results, as shown in Fig. 8e, are consistent with the excellent rate capability and high specific capacitance observed in GCD and CV measurements, confirming the suitability of the modified electrode for high-performance electrochemical capacitor applications.

4 Conclusion

In summary, a hierarchical ZIF-67@NiS-NiF binder-free electrode was successfully developed, demonstrating outstanding electrochemical capacitor performance. The rational integration of ZIF-67 with NiS on a three-dimensional nickel foam substrate provided abundant electroactive sites, enhanced electrical conductivity, and facilitated rapid ion transport. Comprehensive structural and surface characterizations confirmed the successful fabrication and favorable physicochemical properties of the composite electrode. Electrochemical evaluations revealed high specific capacitance, good rate capability, and excellent long-term cycling stability, underscoring the effectiveness of the synergistic ZIF-67/NiS architecture. These results indicate that ZIF-67@NiS-NiF is a promising electrode material for advanced electrochemical energy storage systems and offers a viable strategy for designing high-performance, binder-free supercapacitor electrodes.

Conflicts of interest

The authors declare that there is no conflict of interest regarding the publication of this paper.

Data availability

The datasets used and analyzed during the current study are available from the corresponding author upon reasonable request.

Acknowledgements

The authors extend their sincere appreciation to "Princess Nourah bint Abdulrahman University Researchers Supporting Project number (PNURSP2026R107), Princess Nourah bint Abdulrahman University, Riyadh, Saudi Arabia".

References

1 D. G. Ockwell, Energy and economic growth: Grounding our understanding in physical reality, *Energy Policy*, 2008, **36**, 4600–4604.
2 C. Pasten and J. C. Santamarina, Energy and quality of life, *Energy Policy*, 2012, **49**, 468–476.
3 D. I. Stern, The role of energy in economic growth, *Ann. N. Y. Acad. Sci.*, 2011, **1219**, 26–51.
4 J. P. Dorian, H. T. Franssen and D. R. Simbeck, Global challenges in energy, *Energy Policy*, 2006, **34**, 1984–1991.
5 A. Rashedi, T. Khanam and M. Jonkman, On reduced consumption of fossil fuels in 2020 and its consequences in global environment and exergy demand, *Energies*, 2020, **13**, 6048.
6 M. F. Rabbi, J. Popp, D. Máté and S. Kovács, Energy security and energy transition to achieve carbon neutrality, *Energies*, 2022, **15**, 8126.
7 O. M. Mohammed, Renewable energy: sources, integration and application, *J. Eng. Res. Reports*, 2021, **20**, 143–161.
8 A. Haldorai, A Survey of Renewable Energy Sources and their Contribution to Sustainable Development, *J. Enterp. Bus. Intell.*, 2022, **2**, 211–222.
9 O. Bashiru, C. Ochem, L. A. Enyejo, H. N. N. Manuel and T. O. Adeoye, The crucial role of renewable energy in achieving the sustainable development goals for cleaner energy, Glob, *J. Eng. Technol. Adv.*, 2024, **19**, 11–36.

10 D. Gayen, R. Chatterjee and S. Roy, A review on environmental impacts of renewable energy for sustainable development, *Int. J. Environ. Sci. Technol.*, 2024, **21**, 5285–5310.
11 S. Kumar and K. Rathore, Renewable energy for sustainable development goal of clean and affordable energy, *Int. J. Mater. Manuf. Sustain. Technol.*, 2023, **2**, 1–15.
12 M. Y. Suberu, M. W. Mustafa and N. Bashir, Energy storage systems for renewable energy power sector integration and mitigation of intermittency, *Renew. Sustain. Energy Rev.*, 2014, **35**, 499–514.
13 S. R. Salkuti, Emerging and advanced green energy technologies for sustainable and resilient future grid, *Energies*, 2022, **15**, 6667.
14 M. A. Rahman, J. Kim and S. Hossain, Recent advances of energy storage technologies for grid: A comprehensive review, *Energy Storage*, 2022, **4**, e322.
15 F. H. Malik, G. A. Hussain, Y. M. S. Alsmadi, Z. M. Haider, W. Mansoor and M. Lehtonen, Integrating energy storage technologies with renewable energy sources: a pathway toward sustainable power grids, *Sustainability*, 2025, **17**, 4097.
16 M. Kiasari, M. Ghaffari and H. H. Aly, A comprehensive review of the current status of smart grid technologies for renewable energies integration and future trends: The role of machine learning and energy storage systems, *Energies*, 2024, **17**, 4128.
17 J. Sun, B. Luo and H. Li, A review on the conventional capacitors, supercapacitors, and emerging hybrid ion capacitors: past, present, and future, *Adv. Energy Sustain. Res.*, 2022, **3**, 2100191.
18 W. Liu, X. Sun, X. Yan, Y. Gao, X. Zhang, K. Wang and Y. Ma, Review of energy storage capacitor technology, *Batteries*, 2024, **10**, 271.
19 P. J. Hall, M. Mirzaeian, S. I. Fletcher, F. B. Sillars, A. J. R. Rennie, G. O. Shitta-Bey, G. Wilson, A. Cruden and R. Carter, Energy storage in electrochemical capacitors: designing functional materials to improve performance, *Energy Environ. Sci.*, 2010, **3**, 1238–1251.
20 N. Yang, S. Yu, W. Zhang, H. Cheng, P. Simon and X. Jiang, Electrochemical capacitors with confined redox electrolytes and porous electrodes, *Adv. Mater.*, 2022, **34**, 2202380.
21 Y. M. Volfkovich, Electrochemical supercapacitors (a review), *Russ. J. Electrochem.*, 2021, **57**, 311–347.
22 R. Ahmad, U. A. Khan, N. Iqbal and T. Noor, Zeolitic imidazolate framework (ZIF)-derived porous carbon materials for supercapacitors: an overview, *RSC Adv.*, 2020, **10**, 43733–43750.
23 N. Cheng, L. Ren, X. Xu, Y. Du and S. X. Dou, Recent development of zeolitic imidazolate frameworks (ZIFs) derived porous carbon based materials as electrocatalysts, *Adv. Energy Mater.*, 2018, **8**, 1801257.
24 F. S. Alamro, M. A. Hefnawy, N. S. Al-Kadhi, H. A. Ahmed and S. S. Medany, Synergistic effect of ZIF-8 and NiCo 2 O 4 toward efficient performance for urea electrooxidation, *RSC Adv.*, 2025, **15**, 39616–39629.
25 A. Hosseinian, A. Amjad, R. Hosseinzadeh-Khanmiri, E. Ghorbani-Kalhor, M. Babazadeh and E. Vessally, Nanocomposite of ZIF-67 metal–organic framework with reduced graphene oxide nanosheets for high-performance supercapacitor applications, *J. Mater. Sci. Mater. Electron.*, 2017, **28**, 18040–18048, DOI: 10.1007/s10854-017-7747-z.
26 P. A. K. Reddy, H. Han, K. C. Kim and S. Bae, Synthesis of ZIF-67-derived CoS2@graphitic carbon/reduced graphene oxide for supercapacitor application, *Chem. Eng. J.*, 2023, **471**, 144608, DOI: 10.1016/j.cej.2023.144608.
27 S. A. Ansari, H. M. Kotb and M. M. Ahmad, Wrinkle-shaped nickel sulfide grown on three-dimensional nickel foam: A binder-free electrode designed for high-performance electrochemical supercapacitor applications, *Crystals*, 2022, **12**, 757.
28 R. Pothu, R. Bolagam, Q.-H. Wang, W. Ni, J.-F. Cai, X.-X. Peng, Y.-Z. Feng and J.-M. Ma, Nickel sulfide-based energy storage materials for high-performance electrochemical capacitors, *Rare Met.*, 2021, **40**, 353–373.
29 K. D. Ikkurthi, S. S. Rao, J.-W. Ahn, C. D. Sunesh and H.-J. Kim, A cabbage leaf like nanostructure of a NiS@ ZnS composite on Ni foam with excellent electrochemical performance for supercapacitors, *Dalt. Trans.*, 2019, **48**, 578–586.
30 L. Yu, B. Yang, Q. Liu, J. Liu, X. Wang, D. Song, J. Wang and X. Jing, Interconnected NiS nanosheets supported by nickel foam: soaking fabrication and supercapacitors application, *J. Electroanal. Chem.*, 2015, **739**, 156–163.
31 S. Nandhini, A. Juliet Christina Mary and G. Muralidharan, Facile microwave-hydrothermal synthesis of NiS nanostructures for supercapacitor applications, *Appl. Surf. Sci.*, 2018, **449**, 485–491, DOI: 10.1016/j.apsusc.2018.01.024.
32 A. Asghar, M. I. Yousaf, N. A. Shad, M. Munir Sajid, A. M. Afzal, Y. Javed, A. Razzaq, M. Shariq, Q. Gulfam, M. Sarwar and S. K. Sharma, Enhanced Electrochemical Performance of Hydrothermally Synthesized NiS/ZnS Composites as an Electrode for Super-Capacitors, *J. Clust. Sci.*, 2022, **33**, 2325–2335, DOI: 10.1007/s10876-021-02157-7.
33 X. Hu, X. Tian, Y.-W. Lin and Z. Wang, Nickel foam and stainless steel mesh as electrocatalysts for hydrogen evolution reaction, oxygen evolution reaction and overall water splitting in alkaline media, *RSC Adv.*, 2019, **9**, 31563–31571, DOI: 10.1039/C9RA07258F.
34 Y. Dong, G. Zhang, Q. Liu, C. Qi, X. Jiang and D. Gao, Defect chemistry of NiS for oxygen evolution reaction, *J. Alloys Compd.*, 2022, **923**, 166438, DOI: 10.1016/j.jallcom.2022.166438.
35 W. Hou, Y. Huang and X. Liu, Highly Efficient and Recyclable ZIF-67 Catalyst for the Degradation of Tetracycline, *Catal. Lett.*, 2020, **150**, 3017–3022, DOI: 10.1007/s10562-020-03210-2.
36 S. Sundriyal, V. Shrivastav, H. Kaur, S. Mishra and A. Deep, High-Performance Symmetrical Supercapacitor with a Combination of a ZIF-67/rGO Composite Electrode and a Redox Additive Electrolyte, *ACS Omega*, 2018, **3**, 17348–17358, DOI: 10.1021/acsomega.8b02065.

37 F. S. Alamro, M. A. Hefnawy, N. S. Al-Kadhi, H. A. Ahmed and S. S. Medany, Designing CuMn2O4-chitosan composites to enhance capacitance in organic-medium, *J. Phys. Chem. Solids*, 2026, **209**, 113312, DOI: 10.1016/j.jpcs.2025.113312.

38 J. Dai, C. Li, S. Xiao, J. Liu, J. He, J. Li, L. Wang and J. Lei, Fabrication of novel ZIF-67 Composite Microspheres for Effective Adsorption and Solid-phase Extraction of Dyes from Water, *ChemistrySelect*, 2018, **3**, 5833–5842, DOI: 10.1002/slct.201800778.

39 J. Li, W. Li, G. Liu, Y. Deng, J. Yang and Y. Chen, Tricobalt tetraoxide-supported palladium catalyst derived from metal organic frameworks for complete benzene oxidation, *Catal. Lett.*, 2016, **146**, 1300–1308, DOI: 10.1007/s10562-016-1753-2.

40 C. Wu, D. Xie, Y. Mei, Z. Xiu, K. M. Poduska, D. Li, B. Xu and D. Sun, Unveiling the thermolysis natures of ZIF-8 and ZIF-67 by employing in situ structural characterization studies, *Phys. Chem. Chem. Phys.*, 2019, **21**, 17571–17577.

41 P. Martían-Zarza, J. M. Arrieta, M. C. Muñoz-Roca and P. Gili, Synthesis and characterization of new octamolybdates containing imidazole, 1-methyl- or 2-methyl-imidazole co-ordinatively bound to molybdenum, *J. Chem. Soc., Dalton Trans.*, 1993, 1551–1557, DOI: 10.1039/DT9930001551.

42 B. Hachuła, M. Nowak and J. Kusz, Crystal and Molecular Structure Analysis of 2-Methylimidazole, *J. Chem. Crystallogr.*, 2010, **40**, 201–206, DOI: 10.1007/s10870-009-9634-9.

43 H. Park, D. Amaranatha Reddy, Y. Kim, R. Ma, J. Choi, T. K. Kim and K.-S. Lee, Zeolitic imidazolate framework-67 (ZIF-67) rhombic dodecahedrons as full-spectrum light harvesting photocatalyst for environmental remediation, *Solid State Sci.*, 2016, **62**, 82–89, DOI: 10.1016/j.solidstatesciences.2016.10.018.

44 T. Truong, T. M. Hoang, C. K. Nguyen, Q. T. N. Huynh and N. T. S. Phan, Expanding applications of zeolite imidazolate frameworks in catalysis: synthesis of quinazolines using ZIF-67 as an efficient heterogeneous catalyst, *RSC Adv.*, 2015, **5**, 24769–24776.

45 B. Bakar, G. Dik, A. Ulu and B. Ateş, Immobilization of xylanase into zeolitic imidazolate framework-67 (ZIF-67) and manganese-doped ZIF-67 (Mn/ZIF-67): A comparison study, *Top. Catal.*, 2024, **67**, 698–713.

46 N. Ezzat, M. A. Hefnawy, S. A. Fadlallah, R. M. El-Sherif and S. S. Medany, Synthesis of nickel-sphere coated Ni-Mn layer for efficient electrochemical detection of urea, *Sci. Rep.*, 2024, **14**, 14818, DOI: 10.1038/s41598-024-64707-z.

47 S. S. Medany, M. A. Hefnawy, S. A. Fadlallah and R. M. El-Sherif, Zinc oxide–chitosan matrix for efficient electrochemical sensing of acetaminophen, *Chem. Pap.*, 2024, **78**, 3049–3061, DOI: 10.1007/s11696-023-03292-3.

48 N. Ezzat, M. A. Hefnawy, S. S. Medany, R. M. El-Sherif and S. A. Fadlallah, Green synthesis of Ag nanoparticle supported on graphene oxide for efficient nitrite sensing in a water sample, *Sci. Rep.*, 2023, **13**, 19441, DOI: 10.1038/s41598-023-46409-0.

49 P. Ning, X. Duan, X. Ju, X. Lin, X. Tong, X. Pan, T. Wang and Q. Li, Facile synthesis of carbon nanofibers/MnO2 nanosheets as high-performance electrodes for asymmetric supercapacitors, *Electrochim. Acta*, 2016, **210**, 754–761, DOI: 10.1016/j.electacta.2016.05.214.

50 Z. Wei, J. Yuan, S. Tang, D. Wu and L. Wu, Porous nanorods of nickel–cobalt double hydroxide prepared by electrochemical co-deposition for high-performance supercapacitors, *J. Colloid Interface Sci.*, 2019, **542**, 15–22, DOI: 10.1016/j.jcis.2019.01.114.

51 F. Wang, S. Sun, Y. Xu, T. Wang, R. Yu and H. Li, High performance asymmetric supercapacitor based on Cobalt Nickle Iron-layered double hydroxide/carbon nanofibres and activated carbon, *Sci. Rep.*, 2017, **7**, 4707, DOI: 10.1038/s41598-017-04807-1.

52 A. H. Bashal, M. A. Hefnawy, H. A. Ahmed, M. A. El-Atawy, R. A. Pashameah and S. S. Medany, Green Synthesis of NiFe2O4 Nano-Spinel Oxide-Decorated Carbon Nanotubes for Efficient Capacitive Performance—Effect of Electrolyte Concentration, *Nanomaterials*, 2023, **13**(19), 2643, DOI: 10.3390/nano13192643.

53 M. A. Hefnawy, R. Abdel-Gaber, S. M. Gomha, M. E. A. Zaki and S. S. Medany, Synthesis of Nickel-Manganese Spinel Oxide Supported on Carbon-Felt Surface to Enhance Electrochemical Capacitor Performance, *Electrocatalysis*, 2025, **16**, 500–512, DOI: 10.1007/s12678-025-00932-y.